1990-10-01

The effect of externally applied oscillating electric fields on the l=1 and l=2 diocotron modes in non-neutral plasmas

Ross L. Spencer
ross_spencer@byu.edu

The effect of externally applied oscillating electric fields on the $l=1$ and $l=2$ diocotron modes in non-neutral plasmas

Ross L. Spencer
Department of Physics and Astronomy, Brigham Young University, Provo, Utah 84602

(Received 1 December 1989; accepted 19 June 1990)

A high-frequency oscillating electric field can change the properties of diocotron modes in non-neutral plasmas. The effect depends crucially on the azimuthal mode number, m, of the applied field. For $m = 0, \pm 1$ there is no effect, and for applied standing waves there is also no effect. But if the applied field has the form of a traveling wave with $|m| \geqslant 2$, the frequency of stable diocotron modes can be modified and for $|m| \geqslant 3$, the $l = 2$ instability of hollow density profiles can be stabilized. The analytic results are verified with a nonlinear fluid simulation of an infinitely long non-neutral plasma.

I. INTRODUCTION

One of the more interesting ideas encountered in the study of mechanics is that high-frequency oscillating forces can drastically change the behavior of physical systems. The most famous example of such an effect is the dynamically stabilized pendulum, in which the normally unstable upward equilibrium position of a rigid pendulum can be made stable if the point of support is vibrated vertically with sufficient amplitude and frequency.[1] Because of its potential for stabilization, this effect has also been extensively studied in plasmas and fluids.[2–7] Of special interest are the experimental fluid Rayleigh–Taylor instability paper of Wolf[8] and the review paper of Berge.[9] It would appear, however, that this idea has never been investigated for the non-neutral plasmas that have become so interesting through the work of Malmberg and his co-workers.[10] In this paper the effect of high-frequency electrostatic fields on the $l = 1$ and $l = 2$ diocotron modes[11–13] of non-neutral plasmas will be studied.

It will be supposed that the geometry consists of an infinitely long cylinder of radius a, to which an electrostatic potential of the $\phi = \phi_0 \exp[i(m\theta - \Omega t)]$ is applied. This cylinder contains a non-neutral plasma immersed in a strong uniform magnetic field directed along the axis of the cylinder. The modification of the dynamic properties of a non-neutral plasma produced by such a potential is the subject of this paper.

In Sec. II the fluid model used to discuss this situation is described and the result of applying the separation of time scales theory described by Landau and Lifshitz[1] to this plasma is discussed. It is shown that the traveling-wave form for the potential, given above, is crucial; standing-wave forms give no effect to lowest order. It is also shown that for $m = 0$ and for $m = \pm 1$, there is no effect on the dynamics. However, for $|m| \geqslant 2$, the applied field can substantially shift the frequency of stable diocotron modes and for $|m| \geqslant 3$ it can stabilize the $l = 2$ instability that plagues hollow density profiles. In Sec. III a nonlinear fluid simulation is discussed that was used to test the analytic theory of Sec. II. The simulation and the analytic theory are found to be in reasonable agreement. In Sec. IV we conclude the paper and in the Appendix we demonstrate that the dynamic effects discussed in this paper are mainly produced by a ponderomotive drift of the particles that make up the plasma.

II. SEPARATION OF TIME SCALES

It will be assumed that the magnetic field confining the non-neutral plasma is so strong that inertial effects are unimportant. This requires that the applied frequency and the natural mode frequencies be much smaller than the cyclotron frequency. It will also be assumed that everything is uniform along the length of the cylinder so that we only have to study the dynamics in a cross-sectional plane. Under these conditions, the plasma dynamics are governed only by the equations of electrostatics and the $\mathbf{E}\times\mathbf{B}$ drift:

$$\nabla^2\phi = -(q/\epsilon_0)n, \tag{1}$$

$$\mathbf{v} = (-\nabla\phi\times\hat{\mathbf{z}})/B, \tag{2}$$

and

$$\frac{\partial n}{\partial t} + \mathbf{v}\cdot\nabla n = 0, \tag{3}$$

where ϕ is the electrostatic potential, n is the number density, q is the charge on each particle in the fluid, $\mathbf{v}$ is the fluid velocity, B is the magnitude of the confining magnetic field, and $\hat{\mathbf{z}}$ is a unit vector pointing along the long axis of the cylinder. The boundary conditions on the electrostatic potential are to be applied at the radius of the conducting cylinder, $r = a$. The continuity equation, Eq. (3), has the simple form given here because the fluid velocity given in Eq. (2) is incompressible ($\nabla\cdot\mathbf{v} = 0$).

These equations are analyzed by making a separation of time scales. It is assumed that n and ϕ are made up of two different components. One is the "slow" component with a frequency on the order of the equilibrium rotation frequency $\omega_0 \sim v_\theta/r$. The other is a "fast" component with a frequency on the order of the frequency of the applied potential, $\Omega \gg \omega_0$. Hence we write

$$n = N + \nu \tag{4}$$

and

$$\phi = F + f + f_e, \tag{5}$$

where N and F are the "slow" components and where ν, f, and f_e are the "fast components". For convenience, the "fast" component of the potential has been further split into two parts, one due to the "fast" component of the density and one due to the applied field:

 0899-8221/90/102306-09$02.00

$$\nabla^2 f = -(q/\epsilon_0)\nu, \tag{6}$$

with $f = 0$ at $r = a$, and

$$\nabla^2 f_e = 0, \tag{7}$$

with $f_e = \phi_0 \exp[i(m\theta - \Omega t)]$ at $r = a$.

These forms for n and ϕ are now substituted into Eqs. (2) and (3). By grouping "fast" and "slow" terms together, and by neglecting the high-frequency parts of products of "fast" terms, we get two separate equations (see Ref. 1). It is further assumed that $f \ll f_e$, a condition that can be shown to be equivalent to $\omega_0 \ll \Omega$. With these assumptions, a very simple approximate equation for ν is obtained,

$$\nu = [(\hat{z}\nabla f_e \times \hat{z})/B\Omega] \cdot \nabla N. \tag{8}$$

Since f_e is simply the solution of Eq. (7), we have

$$f_e(r,\theta) = \phi_0 g(r) \exp[i(m\theta - \Omega t)], \tag{9}$$

where

$$g(r) = (r/a)^{|m|}, \tag{10}$$

so that the "fast" density is given by

$$\nu = -\frac{\phi_0}{B\Omega}\left(i\frac{g'(r)}{r}\frac{\partial N}{\partial \theta} + \frac{m}{r}g(r)\frac{\partial N}{\partial r}\right)\exp[i(m\theta - \Omega t)]. \tag{11}$$

This form for ν and Eq. (6) can now be used to check the assumption that $f \ll f_e$. A simple calculation shows that $f \sim \omega_0/\Omega f_e$, so the expansion is consistent to lowest order in ω_0/Ω.

We now substitute this form for ν into the continuity equation and time average the resulting equation over the "fast" time scale to obtain a modified "slow" equation,

$$\frac{\partial N}{\partial t} - \frac{\nabla F \times \hat{z}}{B} \cdot \nabla N - \left\langle \frac{\nabla f_e \times \hat{z}}{B} \cdot \nabla \nu \right\rangle = 0, \tag{12}$$

where $\langle\ \rangle$ denotes the time average.

Equations (9) and (11) are now used to perform the time average, giving the following modified continuity equation:

$$\frac{\partial N}{\partial t} - \frac{\nabla F \times \hat{z}}{B} \cdot \nabla N + h_m(r)\frac{\partial N}{\partial \theta} = 0, \tag{13}$$

where

$$h_m(r) = m|m|(|m| - 1)(\phi_0^2/B^2\Omega a^4)\,(r/a)^{2(|m|-2)}. \tag{14}$$

This is a new equation governing the low-frequency behavior of the plasma in the presence of the high-frequency applied fields. It is, of course, only approximate since all terms of order ω_0/Ω have been neglected. It is possible to extend this calculation to higher order, but this, unfortunately, leads to spatial coupling between the "fast" and "slow" problems. The two can no longer be solved separately and simple results are difficult to obtain. Since the simulation shows that this lowest-order calculation provides a reasonable guide to the physics, we shall be content with it.

A. Stable modes

One of the most interesting properties of non-neutral plasmas is that if the plasma is not centered in the conducting cylinder, then it precesses about the cylinder axis. When the shift is small, this motion may be described by linear theory and is called the $l = 1$ diocotron mode. Stable modes with other values of l also exist in these plasmas. It is natural to ask how the high-frequency fields affect these modes. To study the behavior of linear waves in the system described by Eq. (13), we now assume that N and F are given by

$$N = N_0(r) + N_1(r)\exp[i(l\theta - \omega t)] \tag{15}$$

and

$$F = F_0(r) + F_1(r)\exp[i(l\theta - \omega t)], \tag{16}$$

where $N_0(r)$ and $F_0(r)$ are the azimuthally symmetric equilibrium density and potential profiles. It is, of course, assumed that $\omega \ll \Omega$. In this equilibrium state the fluid rotates as a result of the $\mathbf{E}\times\mathbf{B}$ drift at the radius-dependent frequency ω_0:

$$\omega_0(r) = \frac{1}{rB}\frac{\partial F_0}{\partial r}. \tag{17}$$

Note that this is a positive frequency, indicating rotation in the $+\hat{\theta}$ direction, for negative charges and that it is a negative frequency for positive charges. Substituting these forms into Eq. (13) and linearizing gives the mode equation for this system:

$$[\omega - l\omega_0(r) - lh_m(r)]\left(\frac{1}{r}\frac{\partial}{\partial r}r\frac{\partial F_1}{\partial r} - \frac{l^2}{r^2}F_1\right) - \frac{qlN_0'}{\epsilon_0 rB}F_1 = 0. \tag{18}$$

Except for the presence of the term containing h_m, this is simply the standard diocotron mode equation.[12] As noted by one of the referees, this form suggests that the new term represents an additional drift velocity of the plasma. This is, in fact, correct, as the calculation of the ponderomotive drift velocity in the Appendix demonstrates. Note, however, that in the case of strong magnetization discussed here, this drift is not given by the usual ponderomotive force crossed into the magnetic field, but must instead be calculated using the drift approximation.

There are a few simple consequences of Eqs. (14) and (18). (i) Applied fields with $m = 0$ or $m = \pm 1$ have no effect on diocotron modes, since in these cases $h_m = 0$. It is no surprise that $m = 0$ gives no effect since such an applied potential would produce no applied electric field. But it is a little surprising that $m = \pm 1$ has no effect. If we interpret this effect as due to a ponderomotive drift, however, it becomes clear: for $m = \pm 1$ the applied electric field is simply a uniform rotating transverse field, and uniform electric fields do not produce ponderomotive effects. As we shall see later, a fluid simulation confirms this result. (ii) Since the term in Eq. (18) containing h_m is linear in F_1 and since h_m is odd in m, an applied standing wave has no effect, to the order of approximation taken here. This is, of course, because a standing wave is a linear mixture of positive and negative values of m. This result is also discussed in the Appendix and has been confirmed by the fluid simulation. (iii) For $m = \pm 2$, h_m does not vary with radius. Hence, applied traveling waves with $m = \pm 2$ simply shift the frequency of the diocotron modes. An applied field with $m = +2$ will

increase the mode frequency, ω, while an applied field with $m = -2$ will decrease the mode frequency (for a negatively charged plasma). The opposite is true for a positively charged plasma, and the general result is easy to remember: if the applied wave field travels in the direction of the plasma rotation, the mode frequency is increased, while if it travels opposite to the direction of plasma rotation, the mode frequency is decreased. It is important to note that this effect may be made large without producing large density perturbations because $v \sim \phi_0/\Omega$ while $h_m \sim \phi_0^2/\Omega$. Hence, we may choose values of ϕ_0 and Ω that give a small perturbed density, then increase both ϕ_0 and Ω by some factor until h_m has the desired size. Of course, practical considerations limit the effectiveness of this procedure since it is difficult to achieve both high frequencies and high voltages. Note that for properly chosen m and for large enough applied fields and frequencies, this analysis predicts that it should be possible to make $\omega = 0$, i.e., to make a slightly off-axis non-neutral plasma sit at the same off-axis position without precessing. This behavior has, in fact, been observed with the simulation.

If $|m| \geqslant 3$, then Eq. (18) cannot be solved analytically. It is, however, a simple matter to solve this equation numerically and to use the standard shooting method to obtain ω for arbitrary m. This was done for a few different density profiles, and it was discovered that for given values of ϕ_0 and Ω, $|m| = 3$ gives a slightly larger mode frequency shift than does $|m| = 2$, but for $|m| \geqslant 4$ the function $h_m(r)$ is so highly localized near the outer cylinder that the frequency shift decreases with increasing m.

B. The $l=2$ instability

If the non-neutral plasma density profile is sufficiently hollow, it exhibits an $l = 2$ instability that destroys the hollow profile, causing it to evolve to a new equilibrium with a stable profile. Figure 1 displays a fit to an experimentally determined hollow density profile measured at the University of California at San Diego; this profile is known to be unstable to the $l = 2$ mode.[14] In their experiment the conducting cylinder radius was $a = 3.8$ cm and the axial magnetic field had the value $B = 375$ G. The experimentally observed unstable $l = 2$ mode had a real frequency of 212 kHz and a growth rate of 5.9×10^4 sec^{-1}. When the shooting code is applied to this profile, it finds an unstable mode with a real frequency of 202 kHz and a growth rate of 3.6×10^4 sec^{-1}. As discussed in Sec. II A, $m = 2$ external fields applied to such a plasma will just shift the real part of its frequency and have no other effect. However, if an external field with $m = -3$ is applied with sufficient amplitude, the shooting code predicts that this unstable mode can be stabilized. (Note that the negative value of m means that the applied field pattern rotates opposite to the plasma rotation.) For these experimental conditions an applied frequency of $\Omega = 10^7$ sec^{-1} and an applied voltage of $\phi_0 = 30$ V is predicted to give marginal stability with a real frequency of 183 kHz. For reference, this applied potential at the wall is about 2.6 times greater than the plasma potential and the applied frequency is about 7.5 times greater than the real part of the $l = 2$ mode frequency. (Note that if the applied field has $m = +3$, then the growth rate is predicted to increase.) This prediction of stabilization assumes, of course, that no other modes are destabilized by the applied fields and that nonlinear effects do not cause problems. The simulation discussed in the following section indicates that stabilization without such serious side effects can be achieved.

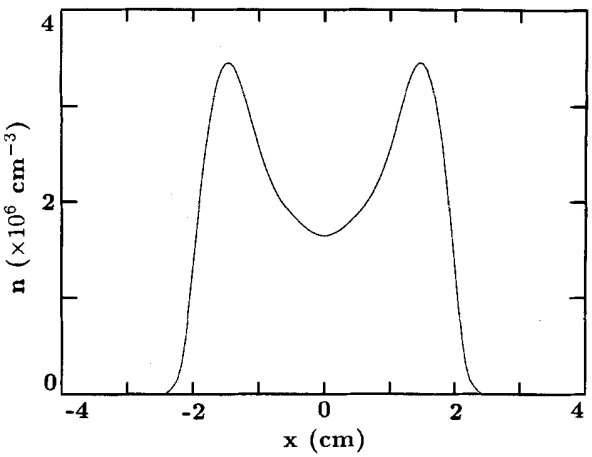

FIG. 1. A fit to an experimentally measured hollow density profile[14] is displayed as a function of position x across a diameter of the conducting cylinder.

III. FLUID SIMULATION

A fluid simulation was written to test these ideas by numerically solving Eqs. (1)–(3). The simulation is based on a Cartesian grid with an inscribed circle representing the cylinder to which the potentials are applied, as shown in Fig. 2. This seems to be awkward, at first glance, because the boundary does not fit the grid, but this scheme is actually an excellent choice. The fluid is expected to have its largest density near the center of the cylinder and its smallest density near the outer cylinder. A cylindrical coordinate system would do a better job of representing the fields in the low density region at the expense of having a singularity ($r = 0$)

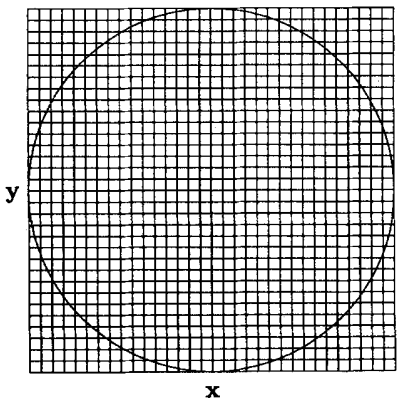

FIG. 2. The computational grid used in the simulation is shown. The external field is produced by specifying the electrostatic potential on the circle. The fluid motion is governed by the $\mathbf{E} \times \mathbf{B}$ drift on the Cartesian grid points within the circle.

right in the middle of the fluid. The Cartesian grid avoids the singularity at the expense of making small errors in the low-density region. Even these errors were minimized by using a first-order accurate representation of ∇^2 for grid points whose five-point star reaches across the circle. And since the fluid stays away from the edge of the cylinder, the continuity equation can be solved using the usual finite-difference techniques for a Cartesian grid. The solution methods for Eqs. (1) and (3) will now be discussed separately in more detail.

Equation (1) is solved by a hybrid method: (1) The Alternating-Direction-Implicit[15] algorithm (ADI) is used for all interior grid points (points whose five-point star is entirely contained within the circle) and (2) Gauss–Seidel[16] is used on points whose five-point star reaches across the circle. Gauss–Seidel was used instead of successive overrelaxation (SOR) because numerical experiments showed that it was best. The two methods were combined by performing ADI in the usual way, but with the horizontal and vertical ADI passes followed by two Gauss–Seidel passes on the boundary points. Care was taken to make sure that the code for both of these numerical methods vectorized on the Convex C-210, and extensive tests against known electrostatic fields were performed.

The density was advanced in time by finite differencing the continuity equation in flux-conservative form using the staggered-leapfrog method.[17] As usual, a little numerical viscosity was added to avoid the mesh drift instability. The resulting equation for the time-advanced density is

$$n_{ij}^{m+1} = (1-\alpha)n_{ij}^{m-1} + (\alpha/4)(n_{i,j+1}^{m} + n_{i+1,j}^{m} + n_{ij-1}^{m} + n_{i-1,j}^{m}) - (\Delta t/2\Delta x^2 B)\left[- n_{i+1,j}^{m}(\phi_{i+1,j+1}^{m} - \phi_{i+1,j-1}^{m}) + n_{i-1,j}^{m}(\phi_{i-1,j+1}^{m} - \phi_{i-1,j-1}^{m}) + n_{ij+1}^{m}(\phi_{i+1,j+1}^{m} - \phi_{i-1,j+1}^{m}) - n_{ij-1}^{m}(\phi_{i+1,j-1}^{m} - \phi_{i-1,j-1}^{m})\right]. \quad (19)$$

In this equation, m denotes the time level, i and j denote horizontal and vertical positions, respectively, on the grid of Fig. 2, Δt is the time step, Δx is the grid spacing, and α is the numerical viscosity coefficient. Since this method requires two previous time levels, the code is started by using a simple first-order accurate method to make an initial step backward in time. Because of initial noise, it was found helpful to have $\alpha \sim 0.1$ for about the first 50 time steps to smooth things out. After this early period, α was reduced to about 10^{-4}. This method is explicit, and so has a Courant condition,

$$E\Delta t/B\Delta x < 1. \quad (20)$$

In practice it is found that for fine grids (say 33×33 or finer) the limit drops from 1 down to about 0.2. A typical large run on a 127×127 grid requires several hours of CPU time on the Convex C-210 and uses about 4000 time steps. The total integrated density in these runs is conserved to better than 1%, in spite of the appearance of negative values of the density near the outer edge of the plasma. These negative densities are typically only a few percent of the maximum density and do not appear to affect the ability of the code to represent the plasma.

A. The $l=1$ mode

To test the ideas of Sec. II, a series of computer runs was made. First, the unmodified $l = 1$ diocotron mode was simulated. Figure 3 shows contours of the initial density, and it can be seen that the initial condition consists of a cylindrically symmetric density distribution shifted to the right. The peak density was $n_0 = 10^{13}$ m^{-3}, the radius was $a = 5$ cm, and the magnetic field was $B = 1$ kG. The simulation was run both with a 33×33 grid and with a 65×65 grid. No appreciable difference was observed between the two cases either in this run or in other similar test runs with applied fields. Hence, in the interest of economy, the runs described in Sec. III A all used a 33×33 grid. A three-dimensional view of the initial density is shown in Fig. 4. (Note: the contour and three-dimensional plots are based on quadratic interpolations to a finer grid.) The simulation was allowed to run for 40 μsec (about 1.2 diocotron mode periods) and the density at each of the positions marked in Fig. 3 was monitored as a function of time. The density at each of the marked points is plotted in Fig. 5 while the final density distribution is shown in Fig. 6. Only about one period of the diocotron mode has been followed, and it is not possible to determine its frequency simply from Fig. 5. However, there is an excellent diagnostic that does determine its frequency very accurately. This quantity is the angular position of the center of mass of the density distribution θ_{cm}. This quantity is plotted for this run in Fig. 7. There is no difficulty in determining that the $l = 1$ diocotron frequency for this simulation is 29.0 kHz. This compares quite favorably with the linear theory, which predicts a mode frequency of 28.5 kHz. Even this discrepancy can be accounted for by noting that for this run

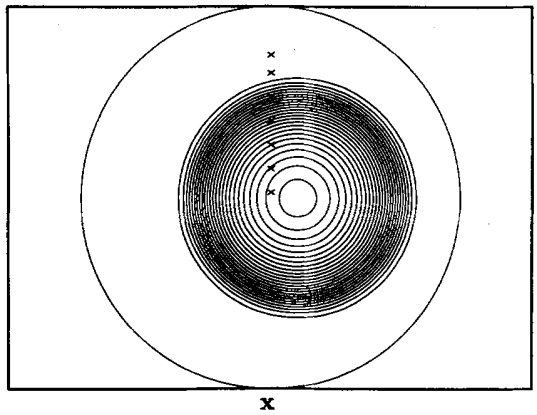

FIG. 3. Contours of constant density are shown at the beginning of the baseline run in which the $l = 1$ diocotron mode is followed without any high-frequency applied electric field. The peak value of the density is 10^{13}m^{-3}. The $\times$'s denote grid points for which the density is monitored as a function of time.

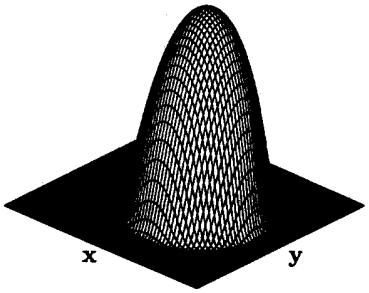

FIG. 4. A three-dimensional representation of the initial density of Fig. 3 is displayed.

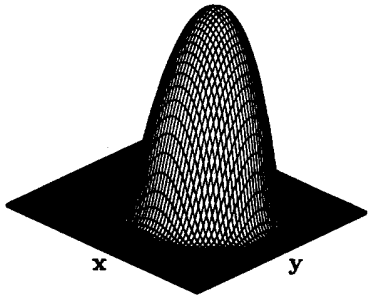

FIG. 6. The density is displayed after the fluid has been allowed to evolve for 40 μsec (about 1.2 periods of the $l = 1$ diocotron mode). The simulation used 800 time steps to reach this time. Note that there are a few ripples outside the main body of the density distribution where the density has become slightly negative, but that on the whole the simulation is remarkably smooth.

the center of the plasma was shifted 15% of the way from the center to the wall. For the density profile used here, the formulas of Ref. 18 predict an upward shift of the frequency by about 0.5 kHz. To make sure this was not fortuitous, a smaller displacement was used, and it gave a frequency closer to 28.5 kHz by the expected amount. Smaller displacements were not used as a matter of course because the center of mass diagnostic does not work well when the center of mass is less than $2\Delta x$ from the center of the cylinder.

The next run in the series was a test to see if an applied $m = +1$ traveling wave has an effect on the diocotron mode. The applied potential at the wall was $\phi_0 = 100$ V and the applied frequency was $\Omega = 7.54 \times 10^6$ rad/sec. This applied potential is about twice the plasma potential and the applied frequency is about 40 times bigger than the diocotron mode frequency, and about eight times bigger than the maximum value of ω_0. The initial density was the same as that for the previous run, displayed in Fig. 3. Figure 8 shows the time variation of the density at the positions shown in Fig. 3, and it is clear that fairly large modulations are taking place. It is also clear that it would be difficult to find the diocotron mode frequency from such a plot. Fortunately, however, the angular position of the center of mass behaves very regularly, as shown in Fig. 9. The diocotron mode frequency given by this figure is 28.5 kHz, hardly changed at all from the 29.0 kHz of Fig. 7. Another run with $m = -1$ gave a simulation mode frequency of 29.4 kHz, also hardly changed from the 29.0 kHz of Fig. 7. Hence the simulation indicates that applied traveling-waves fields do indeed have little effect for $m = \pm 1$, as predicted by the theory of Sec. II.

The cases of $m = \pm 2$ were tried next. The applied potential and frequency were the same as in the $m = +1$ run and the initial density was again the same as in Fig. 3. Figure 10 shows the density at each point in Fig. 2 for $m = +2$. The oscillations appear even more irregular than the case where $m = +1$, and the final density becomes quite distorted, as shown in Fig. 11. However, θ_{cm} still behaves quite nicely, as shown in Fig. 12, and can be used to determine the modified $l = 1$ diocotron mode frequency. Linear theory predicts that the new mode frequency should be 42.0 kHz. The upper trace of Fig. 12 gives a mode frequency of 43.6 kHz, close to the prediction of linear mode theory and representing an increase of nearly 50% above the diocotron mode frequency without applied fields. The lower trace is the re-

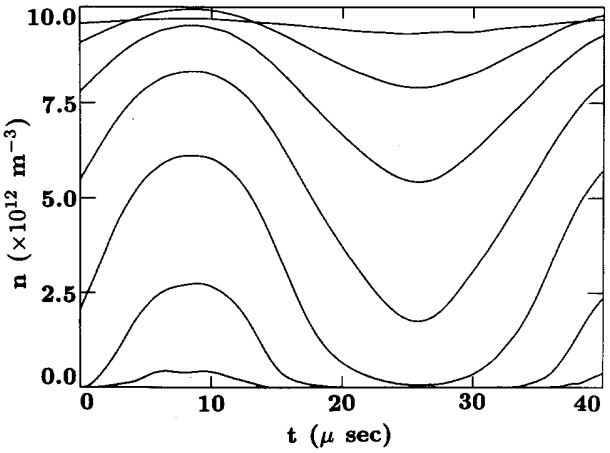

FIG. 5. The density at each of the ×'s in Fig. 3 is displayed as a function of time. The oscillation is the $l = 1$ diocotron mode without oscillating external fields.

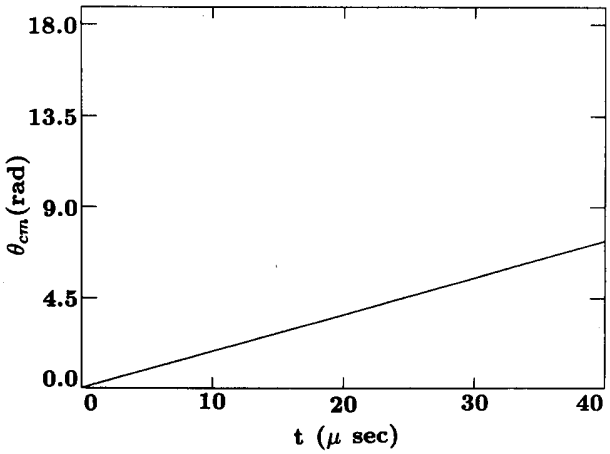

FIG. 7. The angular position of the center of mass of the density distribution is displayed as a function of time during the period when the fluid evolves from Fig. 4 to Fig. 6. This is the quantity which best determines the frequency of the $l = 1$ diocotron mode. The mode frequency obtained from this plot is 29.0 kHz while the predicted mode frequency from linear theory (the equilibrium $\mathbf{E} \times \mathbf{B}$ drift frequency at the wall) is 28.5 kHz.

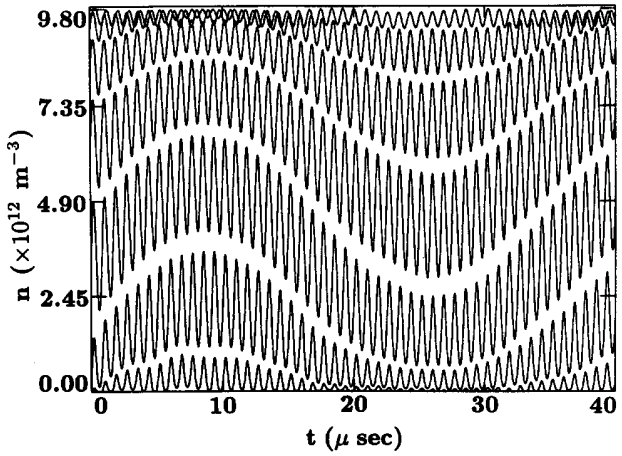

FIG. 8. The density at the ×'s in Fig. 3 as a function of time is displayed for the case where there is an applied external field with wall potential $\phi_0 = 100$ V, applied frequency $\Omega = 7.54 \times 10^6$ rad/sec, and mode number $m = +1$. The applied potential is about twice the plasma potential and the applied frequency is about 40 times as large as the $l = 1$ diocotron mode frequency.

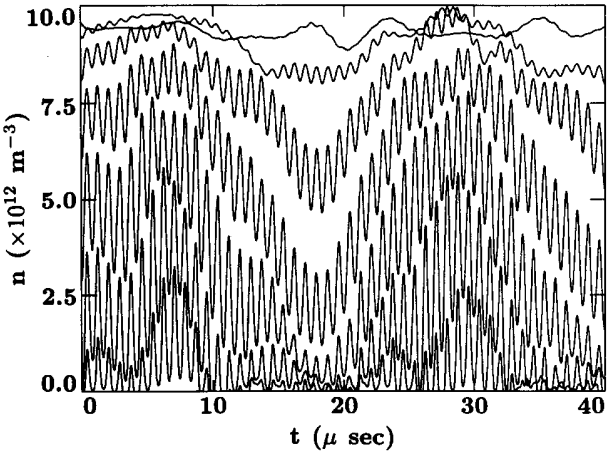

FIG. 10. The density at the ×'s in Fig. 3 as a function of time is displayed for the case where there is an applied external field with wall potential, $\phi_0 = 100$ V, applied frequency $\Omega = 7.54 \times 10^6$ rad/sec, and mode number $m = +2$.

sult of a similar run with $m = -2$, with a simulation frequency of 16.5 kHz (nearly a 50% decrease in frequency), which is to be compared with the linear mode theory prediction of 15.0 kHz. Hence the same applied potential and frequency that had hardly any effect for $m = \pm 1$ had a very large and predictable effect for $m = \pm 2$. It should also be noted that the discrepancies between the simulation and the theory are of about the expected size. For these runs the maximum value of ω_0/Ω was 0.12, and all terms of this order were neglected in the calculations of Sec. II.

The final runs in the $l = 1$ series used $m = \pm 3$. The applied potential and frequency were unchanged from previously described runs. The time variation θ_{cm} for $m = \pm 3$ is shown in Fig. 13. This figure is considerably less regular in its fine features than Fig. 12, but there is still a clear $l = 1$ mode frequency. To find the prediction of the approximate linear theory the shooting method must be used on Eq. (18); it gives for $m = +3$ a diocotron mode frequency of 43.6 kHz, to be compared with the simulation mode frequency of 48.9 kHz (a 70% frequency increase) obtained from the upper trace of Fig. 13. For the case of $m = -3$ shooting predicts of 12.4 kHz while the lower trace of Fig. 13 gives 11.8 kHz (a frequency decrease of 60%). It is clear that in this case the simulation does not agree so well with the analysis of Sec. II. The large discrepancy seems to be caused by the neglect of terms of order ω_0/Ω in Sec. II, many of which are actually of order $m\omega_0/\Omega$, or 0.36 for this case. To test this conjecture other runs were made with the magnitude of $h_m(r)$ held fixed while Ω was increased. It was observed that the mode frequency shift was converging toward a value about 10% higher than the frequency shift predicted by the shooting code. Further runs revealed that this additional shift was caused by the fairly large plasma displacement used to model the $l = 1$ diocotron mode. Instead of the 0.5 kHz increase in frequency caused by the finite displacement without applied fields, an increase of 1.5 kHz is caused by the finite displacement in the $m = 3$ case discussed here. Even though the agreement is poorer, however, the trend is in the right direction and suggests that the time scale separation theory of Sec. II is a useful guide for deciding what happens when high-frequency potentials are applied to such plasmas.

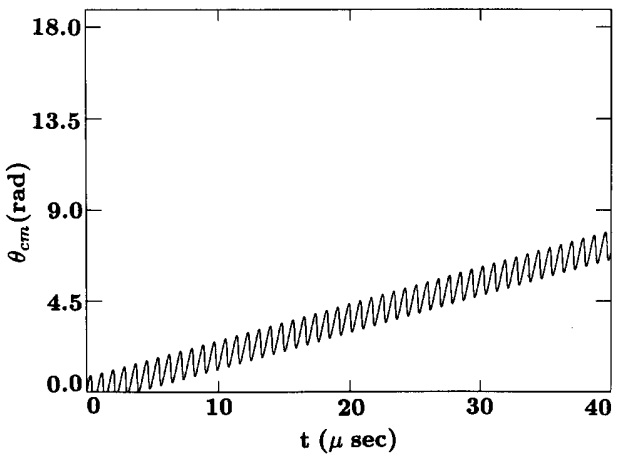

FIG. 9. The angular position of the center of mass of the density distribution for the run of Fig. 8 is displayed. The high-frequency oscillations are the fluid response to the applied fields, while the steady increase in θ_{cm} is the $l = 1$ diocotron mode. The diocotron mode frequency obtained from this plot is 28.5 kHz, essentially unchanged from the 29.0 kHz of Fig. 7, in agreement with the time scale separation theory.

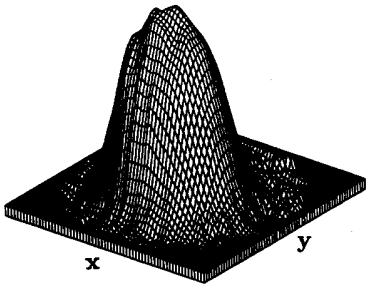

FIG. 11. A three-dimensional view of the final density for the case of Fig. 10 is displayed.

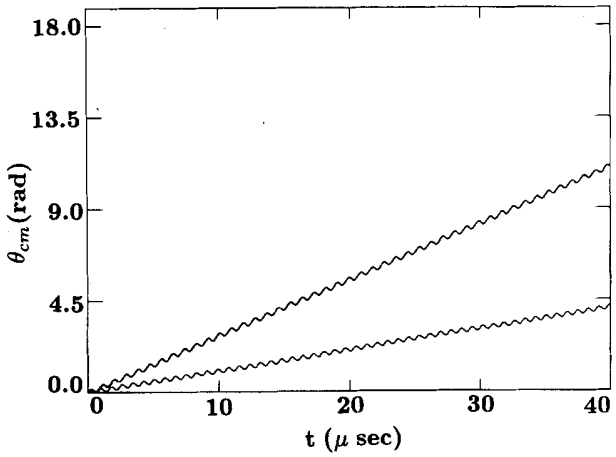

FIG. 12. The upper trace shows the angular position of the center of mass of the density distribution as a function of time for the case of Fig. 10. The $l = 1$ diocotron frequency obtained from this figure is 43.6 kHz, an increase in the mode frequency of nearly 50%, and close to the 42.0 kHz predicted by the time scale separation theory. The lower trace shows θ_{cm} for an applied field with $m = -2$ and all other parameters as given in the caption for Fig. 10. The time scale separation theory predicts an $l = 1$ mode frequency of 15.0 kHz while the frequency obtained from the lower trace is 16.5 kHz, a frequency reduction of about 50%.

B. The $l=2$ instability

The simulation was also used to test the prediction of the shooting code that the $l = 2$ instability for hollow profiles could be stabilized. For these runs the wall radius was $a = 3.8$ cm, the magnetic field was $B = 3375$ G, and a 127×127 grid was used. A finer grid was necessary in these runs because the $l = 2$ mode has a much sharper spatial structure than the $l = 1$ mode. Figure 1 shows the initial density as a function of x through the center of the plasma in

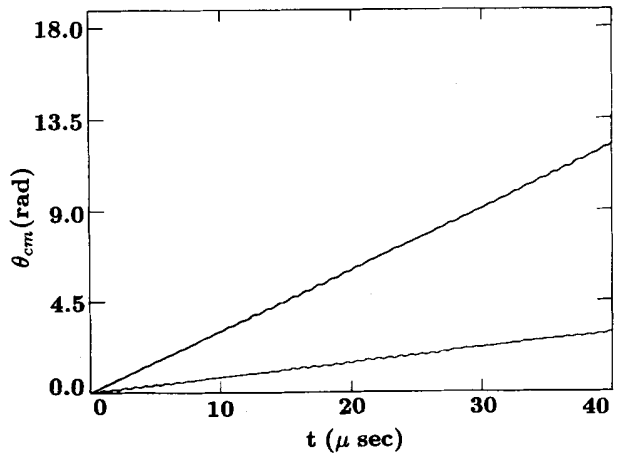

FIG. 13. These two traces show the result of applying fields with $m = \pm 3$ to the system discussed here. The applied potential and applied frequency are as given in the caption for Fig. 8. The upper trace corresponds to $m = +3$. The shooting method applied to Eq. (18) predicts an $l = 1$ mode frequency of 43.6 kHz while the upper trace from the simulation gives a frequency of 48.9 kHz, a frequency increase of nearly 70%. The lower trace corresponds to $m = -3$. The shooting method predicts 12.4 kHz while the lower trace from the simulation gives 11.8 kHz, a frequency reduction of about 60%.

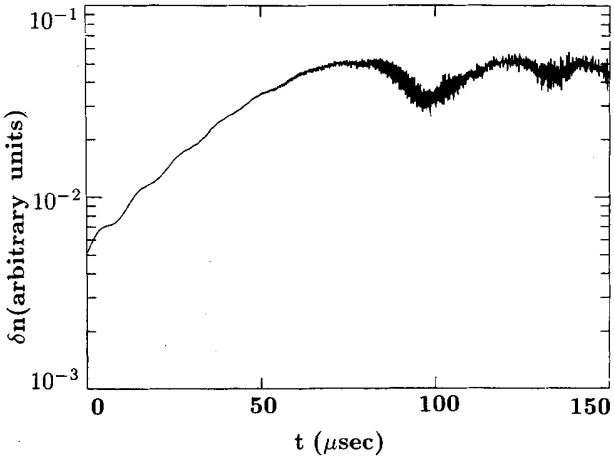

FIG. 14. The $l = 2$ Fourier component of the density, averaged over the fluid, is shown as a function of time for the hollow profile of Fig. 1. The initial perturbation was the eigenfunction from the shooting code. The wall radius was $a = 3.8$ cm, the magnetic field was $B = 375$ G, and a 127×127 grid was used.

the simulation. This density profile is a fit to an experimentally obtained profile that is known to be unstable.[14] The simulation was run for 150 μsec (about five instability growth times) using 5000 time steps and an initial perturbation obtained by having the shooting code compute the unstable density eigenfunction. Figure 14 shows the amplitude of the $l = 2$ Fourier component of the density as a function of time for the case of no applied fields. The nearly exponential growth of this component is within a few percent of the linear growth rate of 3.6×10^4 sec^{-1}, predicted by the shooting code. The real part of the frequency obtained from the simulation also agrees with the shooting code. Figure 15 shows the same Fourier component for a run with everything the same as in the run for Fig. 14, except that an $m = -3$ travel-

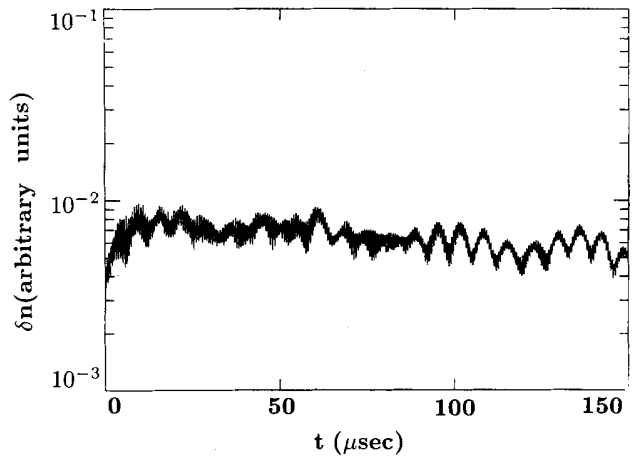

FIG. 15. The $l = 2$ Fourier component of the density, averaged over the fluid, is shown as a function of time for the hollow profile of Fig. 1, but with applied fields. The applied field had $m = -3$, $\Omega = 10^7$sec^{-1}, and $\phi_0 = 40$ V. This applied frequency is 7.5 times greater than the real part of the $l = 2$ mode frequency and this applied potential is 3.5 times larger than the plasma potential. Note that compared to Fig. 14, there is very little growth of the $l = 2$ mode.

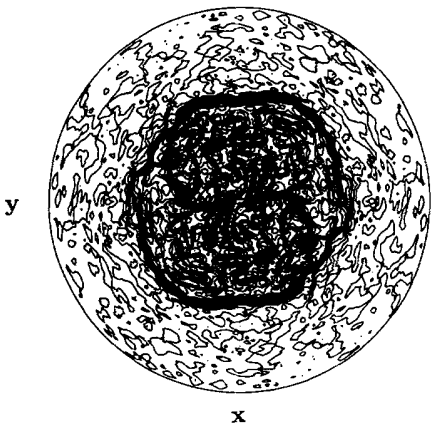

FIG. 16. The density contours at the end of the run without applied fields (Fig. 14) are displayed.

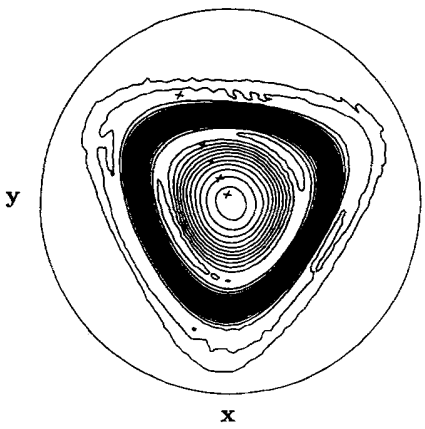

FIG. 17. The density contours at the end of the run with applied fields (Fig. 15) are displayed. Note that although distorted somewhat, this hollow plasma seems to be stable to all modes.

ing wave was applied at the wall. The frequency of the applied potential was $\Omega = 10^7\ \mathrm{sec}^{-1}$ and the amplitude was $\phi_0 = 40$ V, parameters that the shooting code predicted would give stability. For reference, this applied frequency is 7.5 times greater than the real part of the $l = 2$ mode frequency and this applied potential is 3.5 times larger than the plasma potential. The simulation was run for 150 μsec again, but because of the large applied electric fields, 50 000 time steps were required. Note that the instability has been almost completely suppressed. In addition, the plasma density, though somewhat triangular, is very smooth in spite of the applied fields. Figure 16 shows a contour plot of the density after 150 μsec without applied fields while Fig. 17 shows the density at the same time with applied fields. The contrast between these two figures shows that this is apparently a very effective method of stabilization.

IV. CONCLUSION

In the same way that a high-frequency force applied to a pendulum changes its dynamic properties, high-frequency potentials applied to a long non-neutral plasma can change the properties of its normal modes. In particular, traveling-wave patterns with $m \geqslant |2|$ shift the diocotron mode frequencies, and applied fields with $m = -3$ stabilize the $l = 2$ instability that destroys some hollow profile plasmas. The amount of the shift and the stabilization thresholds can be computed by the same time scale separation theory used for the analysis of the dynamic pendulum. These modifications are mainly the result of a ponderomotive drift that modifies the rotation profile of the plasma. Both the predicted frequency shifts and the stabilization of the $l = 2$ mode have been approximately verified by a two-dimensional fluid simulation. The simulation indicates that in spite of the fairly large applied fields, the plasma should remain fairly smooth and hollow. Whether or not this benign behavior would be observed in a real physical system, where transport effects outside the scope of this calculation would play a role, can only be decided by experimentation. It should be noted that this technique would be particularly simple to implement in a beam system where the motion of the plasma could provide the required time dependence if the $m = -3$ potential were applied on a stationary set of helical electrodes at the outer edge.

ACKNOWLEDGMENTS

The author thanks Grant Hart, Dennis Hewett, Neil Rasband, and Bob Webster for helpful discussions and good advice.

APPENDIX: THE PONDEROMOTIVE DRIFT

Here it will be shown that the term h_m in Eq. (18) can be interpreted as the Doppler shift caused by a ponderomotive drift, just as the term ω_0 in the same equation represents the Doppler shift due to the equilibrium $\mathbf{E}\times\mathbf{B}$ drift. The calculation given here differs from the usual derivation of the ponderomotive force[19] in that it is assumed that the magnetic field is so strong that the inertial response of the particles is suppressed. Instead, the particle dynamics is governed by drift motion. Consider a particle in a strong axial magnetic field $B\hat{\mathbf{z}}$ moving under the combined influence of the magnetic field, an oscillating electrostatic field, and a radial electrostatic field produced by a symmetric non-neutral plasma. Assume that the equilibrium drift frequency $\omega_0(r)$, the oscillating electric field frequency Ω, and the cyclotron frequency ω_c, satisfy

$$\omega_0 \ll \Omega \ll \omega_c, \tag{A1}$$

and that the electrostatic potential of the oscillating field has the form

$$\phi = \phi_0 g(r) \exp i(m\theta - \Omega t). \tag{A2}$$

For consistency with Sec. II, effects of order ω_0/Ω will be ignored and the particle dynamics will be assumed to be described by the $\mathbf{E}\times\mathbf{B}$ drift:

$$\mathbf{v} = (\mathbf{E}\times\hat{\mathbf{z}})/B. \tag{A3}$$

Because $\omega_0 \ll \Omega$ the particle will only move a small distance during one period of the applied wave, so we may decompose the position vector of each particle into two parts:

$$\mathbf{r} = r_0 + \boldsymbol{\delta}, \tag{A4}$$

where $|\boldsymbol{\delta}| \ll |\mathbf{r}_0|$. The symbol $\mathbf{r}_0$ denotes the position of the guiding center as it moves under the influence of the low-

frequency drifts, while δ is the relative position vector of the particle, measured from $\mathbf{r}_0$, as it moves due to the high-frequency applied electric field. Because δ is relatively small we may write

$$\dot{\delta} \approx [\mathbf{E}(\mathbf{r}_0,t)\times\hat{\mathbf{z}}]/B, \tag{A5}$$

where $\mathbf{E}$ is the high-frequency electric field, $\mathbf{E}\sim\exp[i(m\theta-\Omega t)]$. Hence, the high-frequency displacement vector is approximately given by

$$\delta \approx (i/\Omega)\{[\mathbf{E}(\mathbf{r}_0,t)\times\hat{\mathbf{z}}]/B\}. \tag{A6}$$

If we now take Eq. (A5) to one more order in δ, a term appears which is a product of rapidly varying quantities and might, therefore, have a nonzero time average corresponding to a low-frequency ponderomotive drift:

$$\dot{\delta} \approx [\mathbf{E}(\mathbf{r}_0,t)\times\hat{\mathbf{z}}]/B + [\delta\cdot\nabla\mathbf{E}(\mathbf{r}_0,t)\times\hat{\mathbf{z}}]/B. \tag{A7}$$

In this approximate equation, δ on the right-hand side is to be taken from Eq. (A6). Taking the time average of the second term yields this drift velocity:

$$\mathbf{v}_{\text{pond}} \approx \tfrac{1}{2}\mathrm{Re}\{[\delta^*\cdot\nabla\mathbf{E}(\mathbf{r}_0,t)\times\hat{\mathbf{z}}]/B\}. \tag{A8}$$

By writing $\mathbf{E}$ in the form

$$\mathbf{E} = \tilde{\mathbf{E}}(r,\theta)e^{-i\Omega t} \tag{A9}$$

and by rearranging the vector products in Eq. (A8) we obtain, finally,

$$\mathbf{v}_{\text{pond}} = (1/2\Omega B^2)\,\mathrm{Im}[\tilde{\mathbf{E}}^*(r,\theta)\cdot\nabla\tilde{\mathbf{E}}(r,\theta)]. \tag{A10}$$

It is now easy to see that standing waves should have no effect, to this order of approximation. Suppose that the applied field had the form of a standing wave; $\tilde{\mathbf{E}}$ would then be real and the ponderomotive drift velocity in Eq. (A10) would be zero.

But if $\mathbf{E}$ is a traveling wave, $\tilde{\mathbf{E}}$ is complex and a nonzero drift velocity results. The drift velocity can be computed by using Eq. (A2) to obtain $\tilde{\mathbf{E}}$,

$$\tilde{\mathbf{E}} = -\phi_0[g'\hat{\mathbf{r}} + (img/r)\hat{\boldsymbol{\theta}}]e^{im\theta}, \tag{A11}$$

and then by substituting Eq. (A11) into Eq. (A10) to obtain

$$\mathbf{v}_{\text{pond}} = \frac{m\phi_0^2}{2\Omega B^2}\left(\frac{g'^2}{r} + m^2\frac{g^2}{r^3} - 2\frac{gg'}{r^2}\right)\hat{\boldsymbol{\theta}}. \tag{A12}$$

Since we are ignoring effects of order ω_0/Ω, g is simply given by the formula for a vacuum electrostatic field,

$$g(r) = (r/a)^{|m|}, \tag{A13}$$

and we obtain for the ponderomotive drift frequency

$$\omega_{\text{pond}} = \frac{\mathbf{v}_{\text{pond}}}{r} = m|m|(|m|-1)\frac{\phi_0^2}{B^2\Omega a^4}\left(\frac{r}{a}\right)^{2(|m|-2)}, \tag{A14}$$

in agreement with Eq. (14) of Sec. II.

Hence, to lowest order in ω_0/Ω the frequency shift and stabilization produced by high-frequency applied electric fields are the result of a ponderomotive modification of the particle drift frequency.

[1] L.D. Landau and E.M. Lifshitz, *Mechanics* (Pergamon, London, 1960), p. 80.
[2] J. Berkowitz, H. Grad, and H. Rubin, in *Proceedings of the 2nd International Conference on the Peaceful Uses of Atomic Energy* (United Nations, Geneva, 1958), Vol. 31, P. 187.
[3] B. A. Trubnikov, Fiz. Plazmy **4**, 309 (1958).
[4] E. S. Weibel, Phys. Fluids **3**, 946 (1960).
[5] F. Troyon, Phys. Fluids **10**, 2660 (1967).
[6] F. A. Haas and J. A. Wesson, Phys. Rev. Lett. **19**, 833 (1967).
[7] F. L. Ribe and W. B. Reisenfield, Phys. Fluids **11**, 2035 (1968).
[8] G. H. Wolf, Z. Phys. **227**, 291 (1969).
[9] G. Berge, Nucl. Fusion **12**, 99 (1972).
[10] J. H. Malmberg and J. S. DeGrassie, Phys. Rev. Lett. **35**, 577 (1975).
[11] R. H. Levy, Phys. Fluids **8**, 1288 (1965).
[12] R. J. Briggs, J. D. Daugherty, and R. H. Levy, Phys. Fluids **13**, 421 (1970).
[13] R. H. Levy, Phys. Fluids **11**, 920 (1968).
[14] C. F. Driscoll (private communication).
[15] W. H. Press, B. P. Flannery, S. A. Teukolsky, and W. T. Vetterling, *Numerical Recipes* (Cambridge U. P., Cambridge, 1986), p. 660.
[16] See Ref. 15.
[17] See Ref. 15.
[18] K. S. Fine, C. F. Driscoll, and J. H. Malmberg, Phys. Rev. Lett. **63**, 2232 (1989).
[19] F. F. Chen, *Introduction to Plasma Physics and Controlled Fusion* (Plenum, New York, 1984), Vol. 1, p. 305.